Journal of Materials Chemistry A

ROYAL SOCIETY OF CHEMISTRY

PAPER

View Article Online
View Journal | View Issue

Check for updates

Cite this: J. Mater. Chem. A, 2024, 12, 7724

Effect of ferroelectric polarization on the oxygen evolution reaction: a theoretical study of $MIrSn_2S_6$ (M = Bi, Mn, and Sb)†

Haoyun Bai, [a] Weng Fai Ip, [b] Wenlin Feng[c] and Hui Pan *[ab]

Received 8th January 2024
Accepted 13th February 2024

DOI: 10.1039/d4ta00152d

rsc.li/materials-a

Ferroelectric polarization plays important roles in catalytic reactions, but the mechanism is still under debate. In this work, 2D ferroelectric $MIrSn_2S_6$ is systematically investigated for revealing the effects of ferroelectric polarization on the oxygen evolution reaction (OER) based on density-functional-theory (DFT) calculations. We find that: (1) the adsorption configurations of intermediates, protons, and water strongly depend on the polarization, which in turn affects their bonding patterns and adsorption energies; (2) the paraelectric (PE) state generally shows the highest OER activity (overpotential = 0.54 V) due to its most favorable free energy change; and (3) the capacitances are varied under different polarization states, which affects the reaction kinetics. Our findings illustrate the full picture of the OER process under different polarizations, which may provide insightful understanding on the ferroelectric-enhanced catalytic activity and guide the design of novel ferroelectric catalysts.

1 Introduction

The development of highly active, long-term stable, and low-cost catalysts has gained increasing attention because of their pivotal role in energy conversion and storage.[1–5] To improve the catalytic performances, various strategies, such as defect engineering,[6,7] composition engineering,[8–10] morphology control,[11–13] strain engineering,[14,15] manipulation of the spin state,[11,16] and modulation of the external field,[17,18] have been developed recently. Especially, the utilization of ferroelectric polarization has been widely explored.[19] For example, perovskites like $BaTiO_3$ showed polarization-dependent adsorption, leading to improved hydrogen evolution reaction (HER).[20–23] The adsorption energies of molecules and the efficiency of CO_2 reduction reaction (CO_2RR) were dependent on the polarization of In_2Se_3.[24,25] Ferroelectricity is also favorable for photocatalysis. For example, perovskites,[26,27] Bi_2WO_6,[28] and $CuInP_2S_6$ [29–31] were applied in photocatalytic water splitting and CO_2RR.

The mechanism of ferroelectric-enhanced catalytic activity has been investigated to guide the design of novel catalysts and improve the efficiency. The polarization changes the surface properties,[22,32] which should affect the adsorption energy of molecules/ions and charge transfer,[20,31,33–35] possibly leading to improved selectivity.[25,36] The tilted band induced by the built-in electric field can significantly accelerate carrier migration and separation, which is beneficial to (photo)catalytic applications, especially in multilayer materials.[29,37,38] In addition, the carrier transportation can be modulated by the ferroelectric polarization as well because of the modified electrode–catalyst contact.[20] The charged surface affects the reaction kinetics too, as indicated by the Tafel slope and reaction impedance.[20,38,39] However, there are still important issues to be addressed. The ferroelectric substrate can only provide limited polarization effect.[40] In contrast, the surface electronic structure strongly depends on the direction and size of polarization in bulk. The stability of polarization in a catalytic environment is unclear. In addition, the coupling among the polarization, spin, and electronic state needs to be discussed. To address these issues, a simple model is necessary.

Recently, a family of two-dimensional (2D) ferroelectric materials, $M_IM_{II}P_2X_6$ (M_I and M_{II} = transition metal, X = S, Se, and Te), has attracted much attention because of its rich composition,[41–43] diverse magnetic and electronic properties,[44–46] and potential application in catalysis.[29,47] When Ge replaces P in $M_IM_{II}P_2X_6$, ferroelectric $M_IM_{II}Ge_2X_6$ (X = S, Se, Te) can be obtained, which further expands the materials' family.[48,49] Especially, the surfaces of paraelectric and ferroelectric phases of $M_IM_{II}Ge_2X_6$ are very similar because the Ge ions protrude from both sides in the paraelectric (PE) phase, and only one Ge ion moves towards the center in the ferroelectric (FE) phase (Fig. 1a and b). $M_IM_{II}Ge_2X_6$ also exhibits rich magnetic and electronic properties,[48,49] which may be used for studying the effect of ferroelectric polarization on the catalytic

[a]Institute of Applied Physics and Materials Engineering, University of Macau, Macao SAR, 999078, P. R. China

[b]Department of Physics and Chemistry, Faculty of Science and Technology, University of Macau, Macao SAR, 999078, P. R. China. E-mail: huipan@um.edu.mo; Fax: +86 853 88222454; Tel: +86 853 88224427

[c]School of Science, Chongqing University of Technology, Chongqing, 400054, P. R. China

† Electronic supplementary information (ESI) available. See DOI: https://doi.org/10.1039/d4ta00152d

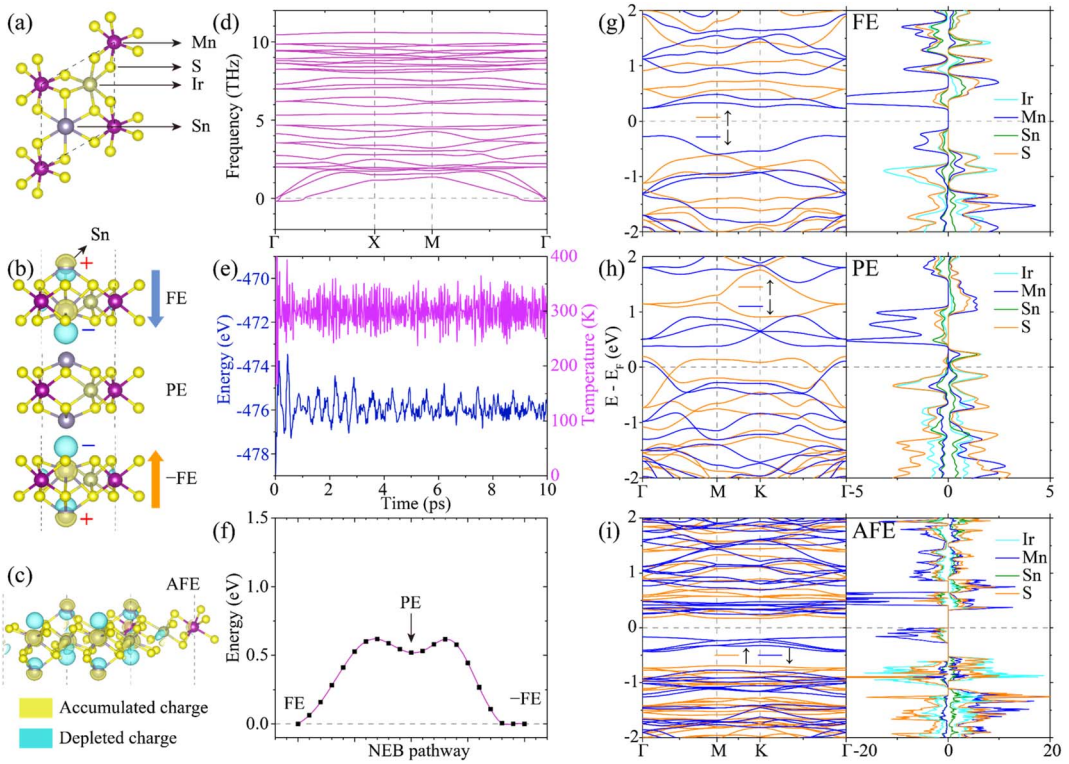

Fig. 1 (a) Top and (b) side views of PE and FE $MnIrSn_2S_6$, and the charge density difference between FE- and PE-$MnIrSn_2S_6$. The arrow represents the direction of polarization. (c) Tilted view of AFE $MnIrSn_2S_6$, and the charge density difference between AFE- and PE-$MnIrSn_2S_6$. (d) Phonon spectrum and (e) AIMD simulation of FE-$MnIrSn_2S_6$. (f) Minimum energy pathway for the phase change of $MnIrSn_2S_6$. Band structures and PDOSs of (g) FE, (h) PE, and (i) AFE-$MnIrSn_2S_6$.

performance. However, the Ge ions are catalytically inactive because the Gibbs free energy change of *OH adsorption is too positive or negative (Fig. S1†). To obtain a series of catalytically active materials with varied electronic properties, we replace Ge with Sn because Sn has strong metallic properties, and been widely used as catalysts in the oxygen evolution reaction (OER). Meanwhile, S and Ir are selected for X and M_{II}, respectively, because this combination shows plentiful electronic properties in $M_IM_{II}Ge_2X_6$.[48,49] Therefore, $M_IM_{II}Sn_2X_6$ is designed to be an ideal model catalyst for the purpose.

In this work, the PE, FE, and anti-ferroelectric (AFE) phases of $MIrSn_2S_6$ (M = Bi, Mn, Sb, and In) are comprehensively studied to determine the role of ferroelectricity in catalytic reactions. We find that the ferroelectricity of PE-$InIrSn_2S_6$ changes in the reaction. For the other three systems, the adsorption configurations in the different phases are distinct. The PE phase generally has the best OER performance due to the most suitable adsorption energy for intermediates, which is attributed to the different bonding patterns between Sn and intermediates. The adsorption energies of H_2O and protons are generally high on the AFE and FE phases. We further show that the capacitances of the three phases are different because their surface charge responds differently to the applied voltage, indicating that the ion transportation in the reaction may be affected by ferroelectricity.

2 Results and discussion

2.1 Structure, stability, magnetic, and electronic properties

The primitive cells of PE- and FE-$MIrSn_2S_6$ (M = Bi, Mn, Sb, and In) are optimized first (Fig. 1a and b). The S ions are located on both sides of $MIrSn_2S_6$. Mn and Ir are sandwiched between the two S layers. The positions of the two Sn ions determine the polarization of $MIrSn_2S_6$: one Sn protrudes from the S layer in the FM phase, while the PE phase has both the Sn ions above the surfaces (Fig. 1b). The electric polarization is also confirmed by the charge density difference between PE- and FE phases (Fig. 1b). The lattice constants of FE and PE phases are similar (Table S1†). The AFE phase is then obtained by using a $2 \times 2 \times 1$ supercell of $MIrSn_2S_6$ (Fig. 1c). PE-$MIrSn_2S_6$ has the highest energy among the three phases, which is consistent with their ferroelectric properties. The AFE state has slightly lower energy than the FE state, except for $SbIrSn_2S_6$ (Table S2†). The formation energies of $MIrSn_2S_6$ are negative, indicating that it is possible to fabricate them (Table S1†). The stabilities of $MIrSn_2S_6$ were also tested. FE-$MIrSn_2S_6$ are all dynamically stable as there are negligible imaginary frequencies around the Γ points in the phonon dispersions (Fig. 1d, and S2a–c†). Meanwhile, huge imaginary frequencies can be seen in PE-$MIrSn_2S_6$, indicating the possible phase change (Fig. S2d†). The calculated elastic constants (Table S3†) and AIMD simulations (Fig. 1e and S3†) further prove that FE-$MIrSn_2S_6$ are

mechanically and thermodynamically stable. The minimum energy pathways between FE- and −FE-$MIrSn_2S_6$ show that the energy barrier is low for the transition from PE to FE phase (Fig. 1f and S4†).

The magnetic and electronic properties of $MIrSn_2S_6$ were then investigated. Only $MnIrSn_2S_6$ is magnetic because of the huge energy difference between the total energies with (E_M) and without (E_{NM}) spin (Table S1†). The magnetic ground states of FE-, PE-, and AFE-$MnIrSn_2S_6$ are ferromagnetic with an exchange energy of over 70 meV per atom (Table S4†). Interestingly, the Mn ion shows a magnetic moment of 2.00 and 2.08 μ_B, respectively, in FE-/AFE- and PE-$MnIrSn_2S_6$ (Table S1†) because of different electronic properties. FE-$MnIrSn_2S_6$ is semiconductive with a band gap of ~1.01/0.50 eV for the spin-up/down channel (Fig. 1g). Mn contributes mostly to the density of states (DOS) around the Fermi level (E_F). PE-$MnIrSn_2S_6$ is conductive (Fig. 1h), and both Mn and S dominate the DOS around E_F. Sn has little contribution to DOS in both FE- and PE-$MnIrSn_2S_6$. AFE-$MnIrSn_2S_6$ is semiconductive and has similar electronic properties to FE-$MnIrSn_2S_6$ (Fig. 1i). The band structure of $InIrSn_2S_6$ is similar to that of $MnIrSn_2S_6$, in which the FE and AFE phases are semiconductive and the PE phase is conductive (Fig. S5†). The three phases of $BiIrSn_2S_6$ and $SbIrSn_2S_6$ are all semiconductive. The PE phase of $BiIrSn_2S_6$ has a much smaller (~0.19 eV) band gap compared to its FE (~1.02 eV) and AFE (~0.89) phase (Fig. S6a–c†). The three phases of $SbIrSn_2S_6$ have a similar band gap of ~0.71 eV (Fig. S6d–f†). The flat bands are mainly contributed by S and Ir around E_F in the band structures for the FE and AFE phases of $BiIrSn_2S_6$ and $SbIrSn_2S_6$ (Fig. S6b, c, e and f†). It is worth noting that the heavy atom Bi leads to strong spin-orbital coupling (SOC), which results in clear band splitting and a band gap of only 0.02 eV in PE-$BiIrSn_2S_6$ (Fig. S7†). Overall, $MIrSn_2S_6$ with special structure and rich electronic properties should provide an ideal platform to study the role of ferroelectricity in catalysis.

2.2 Adsorption under different polarizations

To investigate the OER activity of the PE-, FE-, and AFE-$MIrSn_2S_6$, a 2 × 2 × 1 supercell with a lattice constant of over 12 Å was used. The active sites for the OER were systematically tested first. We find that the protruding Sn ion is the only active site, as *OH always connects to Sn after relaxation whatever the initial adsorption configuration is (Fig. S8†). As Sn is the active sites after testing, the OER cannot happen on the surface of the −FE phase. We find that all three phases for $MnIrSn_2S_6$, $BiIrSn_2S_6$, and $SbIrSn_2S_6$ can maintain their structures during the OER process. The adsorption configurations of *OO and *H on PE-, FE-, and AFE-$MIrSn_2S_6$ are similar. Take $MnIrSn_2S_6$ as an example, the Sn ion moves downward in the PE phase, but has little change in the FE and AFE phases after adsorbing *OO (Fig. 2a). The Sn ion also moves downward slightly after adsorbing *H (Fig. S9†). H_2O cannot adsorb strongly on the surface of $MIrSn_2S_6$ as the distance between Sn and O is over 3 Å (Fig. 2c and S12†). However, the adsorption configurations of *OH, *O, and *OOH are clearly different on PE-, FE-, and AFE-$MIrSn_2S_6$. The Sn ion in the PE phase moves slightly downward,

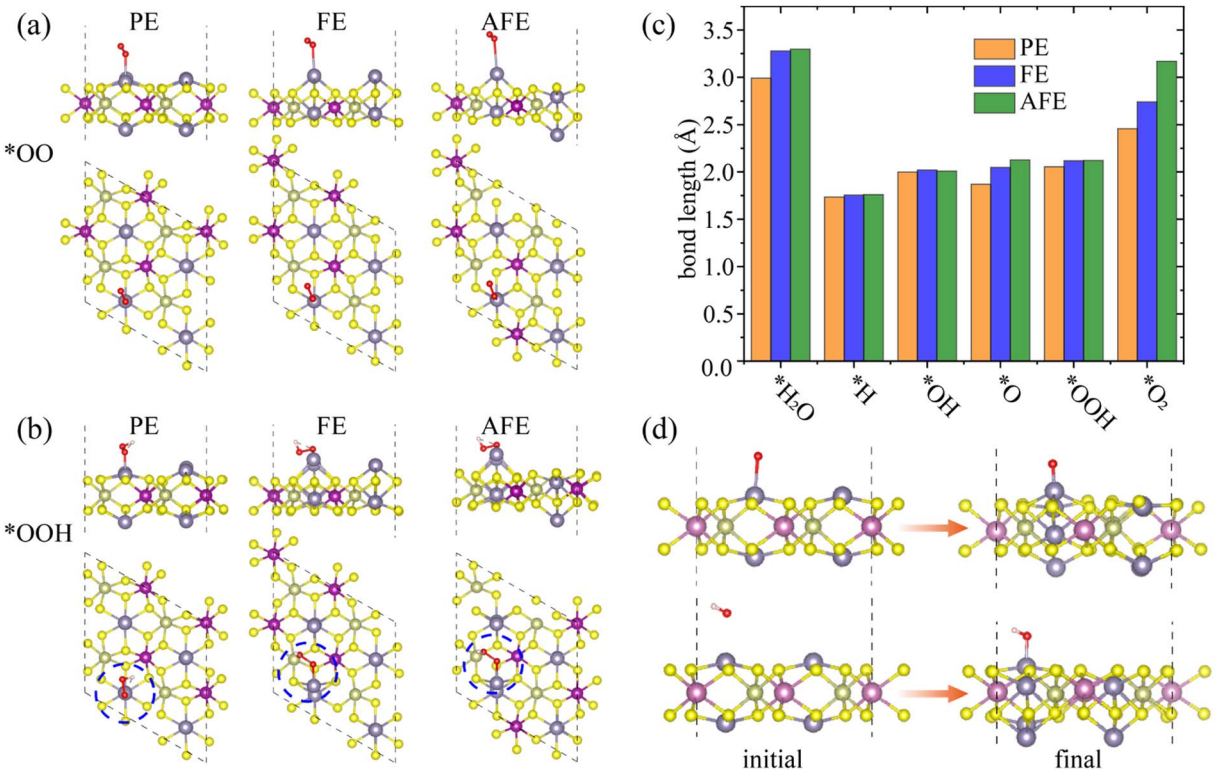

Fig. 2 The adsorption configuration of (a) *OO and (b) *OOH. (c) The comparison of bond lengths between Sn and intermediates on PE, FE, and AFE-$MnIrSn_2S_6$ surfaces. (d) The initial and final structures of *O and *OH adsorption on the PE-$InIrSn_2S_6$ surface.

but is pulled towards another (a neighboring) Sn ion in the FE and AFE phases after *OOH, *O, or *OH is adsorbed (Fig. 2b, S10 and S11†). Specifically, the *O drops on the surface and bonds with S in AFE-$MnIrSn_2S_6$, and connects to the neighboring Sn in FE-$MnIrSn_2S_6$, leading to the movement of Sn (Fig. S11†). The distance between Sn and intermediates (*i.e.*, Sn–O or Sn–H bond) shows the biggest variation in the case of *OO and *H_2O, which are all steps without involving charge transfer. For example, the *OO can weakly adsorb on the top of the Sn ion with a Sn–O bond length of ~2.46 to 3.17 Å in $MnIrSn_2S_6$ (Fig. 2a and c), but the Sn–H and Sn–O bonds in *H and *OH have similar bond length of ~1.75 Å and ~2.00 Å in $MnIrSn_2S_6$ respectively (Fig. 2c, S9 and S10†). The Sn–O bond for the *OOH intermediate in FE-$BiIrSn_2S_6$ is longer than those in the other two phases (Fig. S12†).

Different from $MIrSn_2S_6$ (M = Bi, Mn, and Sb), the PE-$InIrSn_2S_6$ cannot hold its structure in the OER process. The Sn ions bonded with intermediates remain unchanged, but the other Sn atoms on the upper surface move towards the center of the lattice after adsorption, indicating the instability and change of ferroelectric properties in the OER process (Fig. 2d). In addition, the Sn ion connecting with intermediates moves towards the center of the lattice when *OH is adsorbed, while it moves little when *O is adsorbed (Fig. 2d), which may be due to the interaction between the substrate and the intermediates. It is also worth noting that the energy barriers of PE–FE phase change of $InIrSn_2S_6$ and $BiIrSn_2S_6$ are both small (<0.2 eV), but phase change does not occur on PE-$BiIrSn_2S_6$ in the OER process, which may be due to their intrinsic properties (Fig. S4†).

2.3 Adsorption energy and reaction free energy

To obtain the adsorption energies (E_{ad}) of the proton, water molecule, and intermediates in the OER process (*OH, *O, *OOH, and *OO), the spin state is carefully checked.[50] We find that only *OO shows clear spin polarization (Fig. S13 and S19†). The net magnetic moment of *OO is generally 2 μ_B, such as in PE-$MnIrSn_2S_6$, which is consistent with our previous study.[50] However, the net magnetic moment of *OO is ~1.5 μ_B in one excited state in FE-$MnIrSn_2S_6$ (Fig. S13†), which is different from those in PE-$MnIrSn_2S_6$ and the other two substrates. Here, the E_{ad} is calculated by using the ground state energy.

The E_{ad} values of *OOH, *O, and *OH are distinct in $MIrSn_2S_6$ (M = Bi, Mn, and Sb). The E_{ad} values of *O on PE- and FE-$MnIrSn_2S_6$ are nearly 0, but negative on AFE-$MnIrSn_2S_6$ (Fig. 3a). The E_{ad} of *O on PE-$BiIrSn_2S_6$ is still nearly 0, but is −0.57 eV and −1.90 eV on AFE- and FE-$BiIrSn_2S_6$, respectively (Fig. S14a†). FE- and AFE-$SbIrSn_2S_6$ can tightly bond with *O with an E_{ad} of −2.5 eV, but the E_{ad} of *O on PE-$SbIrSn_2S_6$ is only slightly negative (Fig. S15a†). The other intermediates have distinct E_{ad} on different surfaces too. For example, the E_{ad} values of *OH on FE- (−2.08 eV) and AFE-$MnIrSn_2S_6$ (−1.79 eV) are only ~89% and 76% of that on PE-$MnIrSn_2S_6$ (−2.34 eV), respectively (Fig. 3a). The E_{ad} of O_2 on the three phases is similar for $MnIrSn_2S_6$ and $SbIrSn_2S_6$. For the adsorption of O_2 on $BiIrSn_2S_6$, the E_{ad} (−0.20 eV) is negative on the PE surface, but positive on the FE (0.30 eV) and AFE (0.33 eV) surfaces (Fig. S14a†). The adsorption of *H and *H_2O on $MnIrSn_2S_6$ is also significantly different. The *H and *H_2O are adsorbed slightly on the PE-$MnIrSn_2S_6$ surface with an E_{ad} close to ~0 eV. On the other hand, *H and *H_2O show much higher E_{ad} on the FE- and AFE-$MnIrSn_2S_6$ surfaces, indicating difficult adsorption (Fig. 3a). Such differences may also affect the OER performance. However, the E_{ad} values of *H_2O are similar on $BiIrSn_2S_6$ and $SbIrSn_2S_6$. The E_{ad} of *H on PE-$BiIrSn_2S_6$ is significantly lower than that on FE- and AFE-$BiIrSn_2S_6$, but similar on all three phases of $SbIrSn_2S_6$ (Fig. S14a and S15a†).

The contrast E_{ad} corresponds to the distinct Gibbs free energy change in the OER process on the three surfaces. We take $MnIrSn_2S_6$ as an example, the higher E_{ad} values of *OH and *O result in lower Gibbs free energy changes (ΔG) in the first (* + $OH^- \rightarrow$ *OH + e^-) and second (*OH + $OH^- \rightarrow$ *O + H_2O + e^-) steps on the FE and AFE surfaces. However, the huge ΔG in the third (*O + $OH^- \rightarrow$ *OOH + e^-) step leads to the worse OER performances of FE- and AFE-$MnIrSn_2S_6$, which is also the potential determining step (PDS). In contrast, the PDS of PE-$MnIrSn_2S_6$ is the second step, and the three phases of $MnIrSn_2S_6$ have a similar overpotential (~1 V) (Fig. 3b). The second and third steps are the PDS for PE- and AFE-$BiIrSn_2S_6$, respectively, and their overpotentials are similar (~1 V).

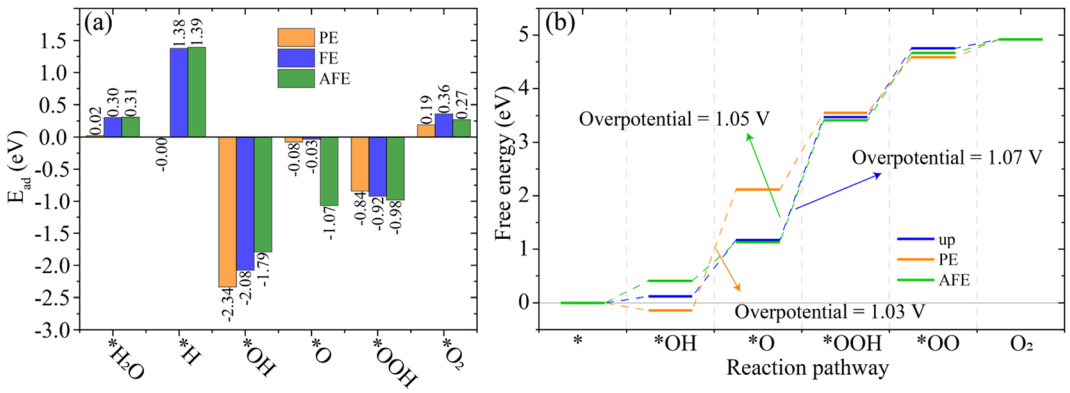

Fig. 3 (a) E_{ad} of intermediates and (b) diagrams of Gibbs free energy change in the OER process on PE-, FE-, and AFE-$MnIrSn_2S_6$. The overpotential is marked in the figure.

Differently, the OER is hard to happen on FE-$BiIrSn_2S_6$ due to the huge ΔG in the third step (Fig. S14b†). FE- and AFE-$SbIrSn_2S_6$ also need to overcome a huge energy barrier in the third step. However, the PE-$SbIrSn_2S_6$ only needs an overpotential of 0.54 V in this step, leading to a good OER performance (Fig. S15b†), which is comparable to those of recognized excellent OER catalysts (Table S5†).

To understand the mechanism, we investigated the bonding of each intermediate by the crystal orbital Hamilton population (COHP) analysis, which illustrates that polarization can affect the bonding patterns. Take the *OH intermediate as an example, the COHP patterns of the Sn–O bond on the FE and AFE surfaces are similar, but distinct from that on the PE state. For example, one antibonding state around −6 eV in the FE and AFE states changes into two in the PE state (Fig. 4a–c). The integration of COHP (ICOHP) on PE-$MnIrSn_2S_6$ is slightly lower than those on FE- and AFE-$MnIrSn_2S_6$, corresponding to the higher E_{ad} of *OH on the PE surface (Fig. 4a–c). Similarly, the Sn–O bonds for the *OOH intermediate in FE and AFE states are clearly distinct from that in the PE state (Fig. S17a†). Specifically, the COHP patterns of Sn–O bonds for the *O intermediate in all three states are different, and the bonding states of the Sn–O bond in AFE-$MnIrSn_2S_6$ are higher than those in FE or PE states, corresponding to the different adsorption configurations of *O. The O–O bonding in *OOH is also affected by polarization (Fig. S17b†). The O–H bonding in *OH and *OOH is also affected in the three states. For example, the shapes of two antibonding states around −7 eV are different in *OH (Fig. 4d–f and S17c†). The Sn–O bonds for the *OO intermediate on the three phases are all different, while the O–O bond of *OO is similar to that in O_2, corresponding to the weak adsorption of O_2 (Fig. S18 and S19†). Spin polarization can be observed in the Sn–O and O–O bonding for *OO, consistent with our previous statements. We also investigated the Sn–H bonding for *H. The COHP patterns of *H are distinct in all three phases. Although the E_{ad} values of *H on the three phases are clearly different, the ICOHPs of Sn–H bonding are similar (Fig. 4g–i).

2.4 Potential–energy relationship and reaction kinetic analysis

Under an external circuit, the surface charge of the electrode is unbalanced, which shall greatly affect the catalytic activity and the kinetics of the OER.[51] When PE-, FE-, and AFE-$MnIrSn_2S_6$ are under a balanced surface charge, the corresponding potentials are also different, and intermediates have complex effects on the surface charge (Fig. 5a–c and S20†). For example, the surface

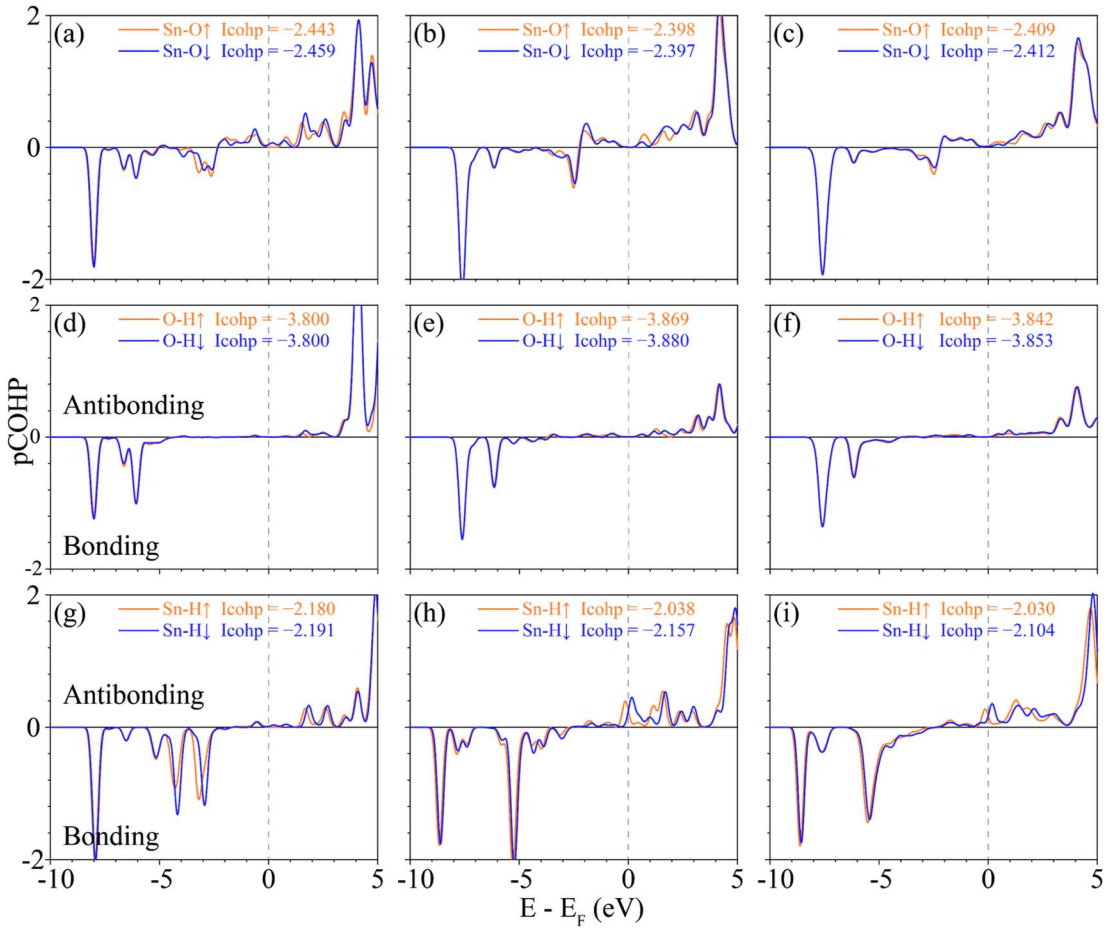

Fig. 4 The COHP of (a–c) Sn–O bonding for the *OH, (d–f) O–H bonding for the *OH, and (g–i) Sn–H bonding for the *H intermediate on (left to right) PE, FE, and AFE-$MnIrSn_2S_6$, respectively.

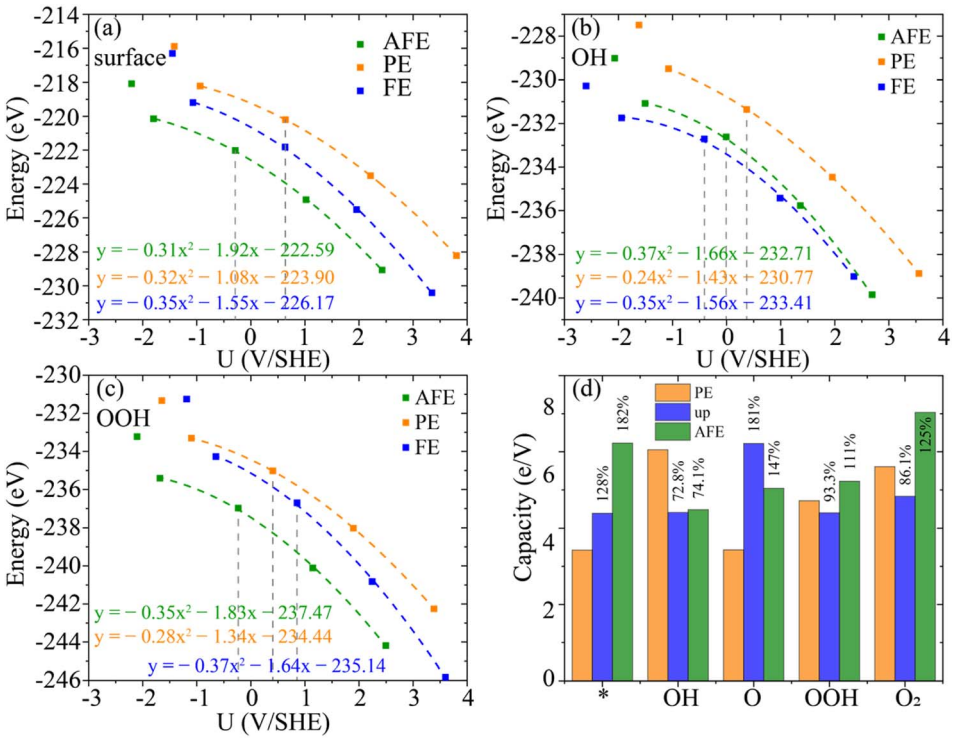

Fig. 5 The potential *vs.* free energy and their fitting of (a) the pure surface, (b) *OH, and (c) *OOH intermediates on PE, FE, and AFE-$MnIrSn_2S_6$. The gray lines indicate the potential when the system has a balanced surface charge. (d) The capacitance of the surface and surface with intermediates. The number represents the percentage relative to the capacitance on the PE surface.

of AFE-$MnIrSn_2S_6$ is negatively charged, but those of FE- and PE-$MnIrSn_2S_6$ are positively charged naturally (Fig. 5a). However, AFE-$MnIrSn_2S_6$ is close to a zero-potential state (−0.007 V *vs.* SHE) when the *OH is adsorbed (Fig. 5b), but a negative potential (−0.23 V *vs.* SHE) can balance the surface charge when *OOH is adsorbed (Fig. 5c). Meanwhile, negative (−0.41 V *vs.* SHE) and positive (+0.37 V *vs.* SHE) potentials are needed, respectively, for FE and PE-$MnIrSn_2S_6$ to have a balanced surface charge when *OH is adsorbed (Fig. 5b), but both positive (+0.41 and +0.86 V *vs.* SHE for PE and FE, respectively) when *OOH is adsorbed (Fig. 5c).

By simulating the relationship between the potential and free energy on $MnIrSn_2S_6$ with each intermediate adsorbed (see also the supplementary notes), we can see the effect of applied potential. When a huge negative potential is applied, the free energies of systems increase dramatically, but the free energy has a good quadratic relationship with potential in the range ∼ −1.5 to 3 V. Thus, the surface capacity can be obtained by fitting the curve (Fig. 5a–c). We can see that the capacitance of the pure surface of $MnIrSn_2S_6$ follows the sequence PE < FE < AFE. However, when the surface is covered by intermediates, the capacitance of PE-$MnIrSn_2S_6$ may get larger than those of the other two phases, such as when *OH is adsorbed (Fig. 5d). Despite the similar OER performance and the COHP pattern of Sn–O, the capacitances of FE- and AFE-$MnIrSn_2S_6$ are also distinct. Specifically, FE-$MnIrSn_2S_6$ has larger surface capacitance for *O, but lower for *OOH and *OO than AFE-$MnIrSn_2S_6$. Take the PE-$MnIrSn_2S_6$ as the reference, the capacitance differences of the three phases can be up to ∼73% and 181% when intermediates are adsorbed, which would affect the kinetic process in the OER greatly (Fig. 5d).

3 Conclusions

In summary, the OER performances of PE-, FE-, and AFE-$MIrSn_2S_6$ are systematically studied. We show that the polarization may change during the OER. The polarization affects the adsorption configuration, which further decides the bonding patterns and adsorption energies of intermediates. PE-$MIrSn_2S_6$ shows the best performance among the three phases, especially for $SbIrSn_2S_6$, which only has an overpotential of 0.54 V. In addition, the adsorption energies of protons and H_2O are significantly different, which may affect the OER activity as well. Finally, the surface charges on PE-, FE-, and AFE-$MIrSn_2S_6$ have a distinct response to potential, resulting in the different capacitances of them, indicating that the kinetic process in the OER may be affected by polarization. Our work not only provided highly active OER catalysts, but also revealed the effect of ferroelectric polarization in catalytic reactions in multiple aspects, which may provide insightful understanding of the reaction mechanism.

4 Computational methods

The first-principles calculations were performed with the Vienna *Ab initio* Simulation Package (VASP) code.[52–54] The

Perdew–Burke–Ernzerhof (PBE) version of the generalized gradient approximation (GGA) was used for the exchange–correlation functional.[55] A vacuum of over 15 Å along the *z*-direction was used to avoid the interaction between neighboring images. The primitive cells of $MIrSn_2S_6$ (M = Bi, Mn, Sb, and In) were first optimized with a plane-wave cutoff energy of 550 eV and a Γ-centered Monkhorst–Pack *k* point mesh of 5 × 5 × 1.[56] The convergence criterion for energy and the force tolerance for ionic relaxation were set as 10^{-6} eV and 0.005 eV $Å^{-1}$, respectively. The formation energies of $MIrSn_2S_6$ were described as $E_f = (E_0 - E_{Ir} - E_M - 2E_{Se} - 6E_S)$, where E_0 is the total energy for $MIrSn_2S_6$, and E_{Ir}, E_M, E_{Se} and E_S are the chemical potentials determined by the most stable Ir, M, Sn crystals and S_8 amorphous, respectively.[57] A 3 × 3 × 1 *k*-mesh was used to obtain the PE, FE, and AFE phases of $MIrSn_2S_6$ in the 2 × 2 × 1 supercell, which is also used for investigation of catalytic performances. The Density-Functional Perturbation Theory (DFPT) method was used to obtain phonon dispersion spectra of $MIrSn_2S_6$ with phonopy code,[58,59] in which the 3 × 3 × 1 supercell and 3 × 3 × 1 Monkhorst–Pack *k*-point sampling were adopted, and the kinetic-energy cutoff was set to 500 eV. The *ab initio* molecular dynamics (AIMD) simulations were carried out with a 3 × 3 × 1 supercell and Γ point at 300 K with a time step of 2 fs.[60] The climbing-image nudged-elastic band (cI-NEB) method is employed to get the ferroelectric switching pathways.[61]

Spin-polarized DFT calculation was performed to study the OER performance of $MIrSn_2S_6$ (M = Bi, Mn, and Sb). The vdW correction of Grimme's D3 scheme was chosen to treat the weak interactions in the system.[62] A *k*-point grid of 3 × 3 × 1, and cut-off energy of 450 eV were used. The convergence thresholds of energy and force were 10^{-5} eV and 0.02 eV $Å^{-1}$, respectively. The adsorption energy of gas molecules was determined by $E_{ad} = E_{sub+gas} - E_{sub} - E_{gas}$, where $E_{sub+gas}$, E_{sub} and E_{gas} are the total energies of the adsorbed system, the substrate and gas molecules, respectively. The Gibbs free energy was calculated as $G = E + ZPE - TS$, where E is the total energy obtained by DFT calculation, and ZPE is zero-point energy, which is calculated as $ZPE = 1/2\sum h\nu_i$, where ν_i is the frequency of intermediates. T is the temperature of reaction, which is set as 298.15 K, and S is entropy. The overpotential of OER *vs.* RHE is defined as $\eta_{ORR} = \max\{\Delta G_i\}/e - 1.23$, where e is the electron charge and ΔG refers to the change of Gibbs free energies in each reaction step. The dipole correction was found to have negligible effect on the trends of the OER performance of systems (Fig. S21†).

Conflicts of interest

The authors declare no conflict of interest.

Acknowledgements

This work was supported by the Science and Technology Development Fund (FDCT) from Macau SAR (0050/2023/RIB2, 0023/2023/AFJ, 006/2022/ALC, and 0111/2022/A2), Multi-Year Research Grants (MYRG-GRG2023-00010-IAPME, and MYRG2022-00026-IAPME) from Research & Development Office at University of Macau, and Shenzhen-Hong Kong-Macao Science and Technology Research Programme (Type C) (SGDX20210823103803017) from Shenzhen. The DFT calculations were performed at the High Performance Computing Cluster (HPCC) of the Information and Communication Technology Office (ICTO) at the University of Macau.

References

1 Z. Y. Yu, Y. Duan, X. Y. Feng, X. Yu, M. R. Gao and S. H. Yu, *Adv. Mater.*, 2021, 2007100.
2 D. Liu, L. Qiao, S. Peng, H. Bai, C. Liu, W. F. Ip, K. H. Lo, H. Liu, K. W. Ng, S. Wang, X. Yang and H. Pan, *Adv. Funct. Mater.*, 2023, **33**, 2303480.
3 D. Liu, R. Tong, Y. Qu, Q. Zhu, X. Zhong, M. Fang, K. Ho Lo, F. Zhang, Y. Ye, Y. Tang, S. Chen, G. Xing and H. Pan, *Appl. Catal., B*, 2020, **267**, 118721.
4 M. Li, Y. Liu, L. Dong, C. Shen, F. Li, M. Huang, C. Ma, B. Yang, X. An and W. Sand, *Sci. Total Environ.*, 2019, **668**, 966–978.
5 M. I. Din, A. G. Nabi, Z. Hussain, R. Khalid, M. Iqbal, M. Arshad, A. Mujahid and T. Hussain, *Int. J. Energy Res.*, 2021, **45**, 8370–8388.
6 Y. Zhu, X. Liu, S. Jin, H. Chen, W. Lee, M. Liu and Y. Chen, *J. Mater. Chem. A*, 2019, **7**, 5875–5897.
7 J. Feng, X. Zhong, M. Chen, P. Zhou, L. Qiao, H. Bai, D. Liu, D. Liu, Y.-Y. Chen, W. F. Ip, S. Chen, J. Ni, D. Liu and H. Pan, *J. Power Sources*, 2023, **561**, 232700.
8 J. Ma, F. Zhu, Y. Pan, H. Zhang, K. Xu, Y. Wang and Y. Chen, *Sep. Purif. Technol.*, 2022, **288**, 120657.
9 M. Qu, X. Ding, Z. Shen, M. Cui, F. E. Oropeza, G. Gorni, V. A. D. L. P. O'Shea, W. Li, D.-C. Qi and K. H. L. Zhang, *Chem. Mater.*, 2021, **33**, 2062–2071.
10 Y. Tian, S. Wang, E. Velasco, Y. Yang, L. Cao, L. Zhang, X. Li, Y. Lin, Q. Zhang and L. Chen, *iScience*, 2020, **23**, 100756.
11 Y. Tong, Y. Guo, P. Chen, H. Liu, M. Zhang, L. Zhang, W. Yan, W. Chu, C. Wu and Y. Xie, *Chem*, 2017, **3**, 812–821.
12 Y. Kong, T. He, A. R. P. Santiago, D. Liu, A. Du, S. Wang and H. Pan, *ChemSusChem*, 2021, **14**, 3257–3266.
13 B. Yang, Y. Wang, B. Gao, L. Zhang and L. Guo, *ACS Catal.*, 2023, **13**, 10364–10374.
14 F. Li, H. Ai, D. Liu, K. H. Lo and H. Pan, *J. Mater. Chem. A*, 2021, **9**(33), 17749–17759.
15 D. Liu, H. Ai, W. T. Lou, F. Li, K. H. Lo, S. Wang and H. Pan, *Sustainable Energy Fuels*, 2020, **4**, 3773–3779.
16 Z. Duan and G. Henkelman, *ACS Catal.*, 2020, **10**, 12148–12155.
17 J. Yao, W. Huang, W. Fang, M. Kuang, N. Jia, H. Ren, D. Liu, C. Lv, C. Liu, J. Xu and Q. Yan, *Small Methods*, 2020, **4**, 2000494.
18 H. Bai, J. Feng, D. Liu, P. Zhou, R. Wu, C. T. Kwok, W. F. Ip, W. Feng, X. Sui, H. Liu and H. Pan, *Small*, 2023, **19**(5), 2205638.
19 W. Ding, J. Lu, X. Tang, L. Kou and L. Liu, *ACS Omega*, 2023, **8**, 6164–6174.
20 P. Abbasi, M. R. Barone, M. d. l. P. Cruz-Jauregui, D. Valdespino-Padilla, H. Paik, T. Kim, L. Kornblum,

D. G. Schlom, T. A. Pascal and D. P. Fenning, *Nano Lett.*, 2022, **22**, 4276–4284.
21 E. S. Beh, S. A. Basun, X. Feng, I. U. Idehenre, D. R. Evans and M. W. Kanan, *Chem. Sci.*, 2017, **8**, 2790–2794.
22 A. Kakekhani and S. Ismail-Beigi, *ACS Catal.*, 2015, **5**, 4537–4545.
23 M. H. Zhao, D. A. Bonnell and J. M. Vohs, *Surf. Sci.*, 2008, **602**, 2849–2855.
24 X. Tang, J. Shang, Y. Gu, A. Du and L. Kou, *J. Mater. Chem. A*, 2020, **8**, 7331–7338.
25 L. Ju, X. Tan, X. Mao, Y. Gu, S. Smith, A. Du, Z. Chen, C. Chen and L. Kou, *Nat. Commun.*, 2021, **12**(1), 5128.
26 G. Huang, G. Zhang, Z. Gao, J. Cao, D. Li, H. Yun and T. Zeng, *J. Alloys Compd.*, 2019, **783**, 943–951.
27 S. Ninova and U. Aschauer, *J. Mater. Chem. A*, 2017, **5**, 11040–11046.
28 G. Zhang, J. Cao, G. Huang, J. Li, D. Li, W. Yao and T. Zeng, *Catal. Sci. Technol.*, 2018, **8**, 6420–6428.
29 Y. Fan, X. Song, H. Ai, W. Li and M. Zhao, *ACS Appl. Mater. Interfaces*, 2021, **13**, 34486–34494.
30 S. Huang, Z. Shuai and D. Wang, *J. Mater. Chem. A*, 2021, **9**, 2734–2741.
31 L. Ju, J. Shang, X. Tang and L. Kou, *J. Am. Chem. Soc.*, 2020, **142**, 1492–1500.
32 K. Garrity, A. Kakekhani, A. Kolpak and S. Ismail-Beigi, *Phys. Rev. B: Condens. Matter Mater. Phys.*, 2013, **88**(4), 045401.
33 S. Sanna, R. Hölscher and W. G. Schmidt, *Phys. Rev. B: Condens. Matter Mater. Phys.*, 2012, **86**(20), 205407.
34 J. H. Lee and A. Selloni, *Phys. Rev. Lett.*, 2014, **112**(19), 196102.
35 I. Efe, N. A. Spaldin and C. Gattinoni, *J. Chem. Phys.*, 2021, **154**, 024702.
36 N. Saito, H. Nishiyama, K. Sato and Y. Inoue, *Surf. Sci.*, 2000, **454–456**, 1099–1103.
37 M. A. Khan, M. A. Nadeem and H. Idriss, *Surf. Sci. Rep.*, 2016, **71**, 1–31.
38 X. Li, Y. Du, L. Ge, C. Hao, Y. Bai, Z. Fu, Y. Lu and Z. Cheng, *Adv. Funct. Mater.*, 2022, 2210194.
39 X. Li, H. Liu, Z. Chen, Q. Wu, Z. Yu, M. Yang, X. Wang, Z. Cheng, Z. Fu and Y. Lu, *Nat. Commun.*, 2019, **10**(1), 1409.
40 K. Garrity, A. M. Kolpak, S. Ismail-Beigi and E. I. Altman, *Adv. Mater.*, 2010, **22**, 2969–2973.
41 R. R. Ma, D. D. Xu, Q. L. Zhong, C. R. Zhong, R. Huang, P. H. Xiang, N. Zhong and C. G. Duan, *Adv. Mater. Interfaces*, 2021, 2101769.
42 S. A. Tawfik, J. R. Reimers, C. Stampfl and M. J. Ford, *J. Phys. Chem. C*, 2018, **122**, 22675–22687.
43 L. Chen, C. Mao, J.-H. Chung, M. B. Stone, A. I. Kolesnikov, X. Wang, N. Murai, B. Gao, O. Delaire and P. Dai, *Nat. Commun.*, 2022, **13**(1), 4037.
44 M. Chyasnavichyus, M. A. Susner, A. V. Ievlev, E. A. Eliseev, S. V. Kalinin, N. Balke, A. N. Morozovska, M. A. Mcguire and P. Maksymovych, *Appl. Phys. Lett.*, 2016, **109**, 172901.
45 Y. Lai, Z. Song, Y. Wan, M. Xue, C. Wang, Y. Ye, L. Dai, Z. Zhang, W. Yang, H. Du and J. Yang, *Nanoscale*, 2019, **11**, 5163–5170.
46 X. Ma, L. Sun, J. Liu, X. Feng, W. Li, J. Hu and M. Zhao, *Phys. Status Solidi RRL*, 2020, **14**, 2000008.
47 L. Ji, L. Chang, Y. Zhang, S. Mou, T. Wang, Y. Luo, Z. Wang and X. Sun, *ACS Catal.*, 2019, **9**, 9721–9725.
48 K.-R. Hao, X.-Y. Ma, Z. Zhang, H.-Y. Lyu, Q.-B. Yan and G. Su, *J. Phys. Chem. Lett.*, 2021, **12**, 10040–10051.
49 X. Y. Ma, H. Y. Lyu, K. R. Hao, Y. M. Zhao, X. Qian, Q. B. Yan and G. Su, *Sci. Bull.*, 2021, **66**, 233–242.
50 H. Bai, D. Liu, P. Zhou, J. Feng, X. Sui, Y. Lu, H. Liu and H. Pan, *J. Mater. Chem. A*, 2022, **10**(47), 25262–25271.
51 H. N. Nong, L. J. Falling, A. Bergmann, M. Klingenhof, H. P. Tran, C. Spöri, R. Mom, J. Timoshenko, G. Zichittella, A. Knop-Gericke, S. Piccinin, J. Pérez-Ramírez, B. R. Cuenya, R. Schlögl, P. Strasser, D. Teschner and T. E. Jones, *Nature*, 2020, **587**, 408–413.
52 W. Kohn and L. J. Sham, *Phys. Rev.*, 1965, **140**, A1133–A1138.
53 P. Hohenberg and W. Kohn, *Phys. Rev.*, 1964, **136**, B864–B871.
54 G. Kresse and J. Furthmüller, *Phys. Rev. B: Condens. Matter Mater. Phys.*, 1996, **54**, 11169–11186.
55 J. P. Perdew, K. Burke and M. Ernzerhof, *Phys. Rev. Lett.*, 1996, **77**, 3865–3868.
56 H. J. Monkhorst and J. D. Pack, *Phys. Rev. B: Solid State*, 1976, **13**, 5188–5192.
57 M. M. Obeid, A. Bafekry, S. U. Rehman and C. V. Nguyen, *Appl. Surf. Sci.*, 2020, **534**, 147607.
58 A. Togo, F. Oba and I. Tanaka, *Phys. Rev. B: Condens. Matter Mater. Phys.*, 2008, **78**(13), 134106.
59 S. Baroni, S. D. Gironcoli, A. D. Corso and P. Giannozzi, *Rev. Mod. Phys.*, 2001, **73**, 515–562.
60 W. G. Hoover, *Phys. Rev. A*, 1985, **31**, 1695–1697.
61 D. Sheppard, P. Xiao, W. Chemelewski, D. D. Johnson and G. Henkelman, *J. Chem. Phys.*, 2012, **136**, 074103.
62 S. Grimme, *J. Comput. Chem.*, 2006, **27**, 1787–1799.